small structures
www.small-structures.com

# Covalently Linked Pigment@$TiO_2$ Hybrid Materials by One-Pot Solvothermal Synthesis

*Frank Sailer, Hipassia M. Moura, Taniya Purkait, Lars Vogelsang, Markus Sauer, Annette Foelske, Rainer F. Winter, Alexandre Ponrouch, and Miriam M. Unterlass**

**Hybrid materials (HMs) combine the high diversity of functionalities of organic compounds with properties typical for inorganic materials, such as high mechanical strength or high thermal stability. Herein, HMs combining organic pigment molecules and $TiO_2$ as inorganic component, with covalently linked components, i.e., so-called class II HMs, are reported. The synthesis of such HMs is intrinsically challenging, as the apolar organic pigment component and the inorganic polar $TiO_2$ component require different conditions for their respective formation. Herein, we circumvent this issue by employing solvothermal synthesis in superheated isopropanol, which through temperature tunability of the solvent properties allows for both generating and linking both components in one-pot. First, it is shown that an organic benzimidazole-based pigment molecule designed for readily binding to Ti can be synthesized solvothermally. Second, new class II titanium-based HMs are generated from $Ti(O^iPr)_4$ and pigment precursors in a solvothermal reaction. The pigment@$TiO_2$ HMs feature significant porosity and are structurally identified as layered structures of lepidocrocite-like $TiO_2$ linked via pigment molecules. These layered HMs assemble into hierarchical nanoflowers, and depending on the pigment segments, different interlayer spacings in between inorganic layers are observed. Third, the pigment@$TiO_2$ materials are shown to be usable as electrode materials in lithium-ion batteries.**

## 1. Introduction

The physiochemical properties of a chemical compound are a consequence of 1) structure and 2) bonding. For instance, organic polymers are typically malleable and lightweight, because 1) structurally they are composed of long chains (enabling entanglement), and 2) their bonding is homopolar covalent between light elements (e.g., C, H, N, O). For generating in one compound new properties synergistically from both the realms of inorganic compounds and organic compounds, the concept of hybrid materials (HMs) has been conceived.[1] Structure and bonding define the properties of HMs: synergistic properties beyond the mere sum of the constituents' properties arise, if new structure and bonding between the components is present in to a sufficient degree, i.e., at a relatively large hybrid interface, to generate new structural patterns. HMs are conventionally subdivided into two categories: 1) class I HMs, exhibiting relatively weak bonding between the inorganic and organic components (i.e., via van der Waals, ionic or hydrogen bonds, hydrophobic–hydrophilic balance), and 2) class II HMs, featuring relatively strong bonding between the components (i.e., covalent or ionocovalent bonds).[1,2] This classification nicely reflects the extent of increasingly synergistic bonding. The majority of HMs contain polymeric metal oxides ($M_xO_y$) as inorganic component (all main group metal oxides are polymeric ionocovalently bonded, except for the alkali and earth alkali $M_xO_y$ and lead oxides) and either a chain polymer or a dye/pigment/small molecule species as organic component. Inorganic matrices containing small organic molecules are mostly inorganic metal oxides containing colorant molecules (the term colorant designates molecules used for their coloring properties). Conventionally one differentiates between "dyes" (dissolved in a solvent or solid matrix) and "pigments" (nanometric solid particles of the colorant that are dispersed in a solvent or solid matrix).[1] These types of HMs are particularly attractive, because they allow for modulating the

F. Sailer, H. M. Moura, L. Vogelsang, R. F. Winter, M. M. Unterlass
Department of Chemistry
University of Konstanz
Universitaetsstrasse 10, 78464 Konstanz, Germany
E-mail: miriam.unterlass@uni-konstanz.de

The ORCID identification number(s) for the author(s) of this article can be found under https://doi.org/10.1002/sstr.202400074.



**DOI: 10.1002/sstr.202400074**

F. Sailer, H. M. Moura, M. M. Unterlass
CeMM-Research Center for Molecular Medicine of the Austrian Academy of Sciences
Lazarettgasse 14, AKH BT 25.3 Vienna, Austria

T. Purkait, A. Ponrouch
Institut de Ciènca de Materials de Barcelona (ICMAB-CSIC)
08193 Bellaterra, Catalonia, Spain

M. Sauer, A. Foelske
Analytical Instrumentation Center
Technische Universitaet Wien
Lehrargasse 6, 1060 Vienna, Austria

materials' optical properties with respect to, e.g., luminescence features or nonlinear optical effects toward laser applications.[3,4] Interestingly, the oldest human-made example of a colorant embedded in an inorganic matrix is Mayan blue, which is composed of the organic pigment indigo (2,2′-bis(2,3-dihydro-3-oxoindolylidene) embedded in a matrix of palygorskite aka attapulgite (a phyllosilicate with the general formula $(Mg,Al)_2Si_4O_{10}(OH)\cdot 4\ H_2O$).[2,5] Mayan blue is a class I HM and exhibits improved color fastness compared to the pristine dye. Countless modern colorant@inorganic matrix HMs have been reported. State-of-the-art metal oxides $M_xO_y$ derived from sol–gel processes are summarized in the following list (class I/II type; colorant; synthesis): $SiO_2$ (class I; porphyrin dyes; sol–gel from silicon alkoxides with premade porphyrins),[6] $ZrO_2$ (class I; porphyrin dyes; impregnation of preformed $ZrO_2$ with organic dyes),[7] $Al_2O_3$ (class I HMs; rhodamine dyes; conversion of $Al(OH)_3/AlCl_3$ to alumina in the presence of premade rhodamine),[8] aluminosilicates (class I; spiropyran dyes; obtained by sol–gel processes in the presence of premade spiropyran dyes),[9] ZnO (class I; Ru–coordination compound dyes; impregnation of ZnO with premade Ru–coordination compound dyes),[10] or $TiO_2$ (class I; Ru–coordination compounds dyes; obtained by impregnating colloidal $TiO_2$ with premade Ru–coordination compound dyes).[11] All the latter examples are class I HMs and are obtained by either a sol–gel process yielding a polymeric metal oxide in the presence of a dye that is for instance dissolved in the solvent in which the sol–gel process is carried out, or, by impregnating a preformed metal oxide with the dye. The latter is a heavily used approach in the field of dye-sensitized solar cells (DSSCs).[7,10] In the DSSC field, strong ionocovalent/covalent linking of dye molecules to semiconducting $M_xO_y$ has been pursued in recent years, through modifying the dye molecules with anchoring groups able to, e.g., coordinate to the metal centers within $M_xO_y$.[12] However, in such DSSCs with covalent dye bonding, the resulting materials feature relatively low dye loading and are merely bound to the surface of sintered $M_xO_y$ particles, but the colorant molecules do not bridge $M_xO_y$ domains or particles. We recently reviewed the state of the art in the field of HMs containing perylene diimides (PDIs aka perylene bisimides) as colorants and $SiO_2$ as matrix.[13] PDIs are prototypical dyes, and $SiO_2$ is the most prototypical sol–gel-derived $M_xO_y$ material. The latter is a direct consequence of the ease of preparation of a wide array of silicon alkoxides and the ease of control over the hydrolysis and condensation kinetics of silicon alkoxides. Sol–gel processes toward essentially all other semimetals and metals are more difficult to control. From our previous comparison, we found that PDI@$SiO_2$ class II hybrids are exclusively obtained from modified silicon alkoxides that already contain the respective premade PDI as one R group. We contributed the first examples of PDI@$SiO_2$ HMs obtained by simultaneous synthesis and linking of the PDI colorant molecules and the $SiO_2$ matrix under hydrothermal conditions.[13] Aside PDI@$SiO_2$ class II HMs, we are aware of one example of a mixed $SiO_2$ and $ZrO_2$ matrix (obtained by a mixed sol–gel process of a PDI-functionalized silicon alkoxide with Zr–isopropoxide) by Müllen and coworkers,[14] and a recent example of a PDI@ZnO class II HM by Würthner and coworkers, obtained by employing a PDI functionalized with four carboxylic acid groups that in a sol–gel preparation of ZnO would coordinate to $Zn^{2+}$ sites as carboxylate ligands.[15,16] Here, we have set out to prepare class II HMs using $TiO_2$ as inorganic component. As organic component, we aimed at perinone pigments bearing carboxylic acid groups, hypothesizing that the carboxylic acid functions would enable strong linking to the $TiO_2$ component as carboxylato ligands. We had earlier reported the synthesis of the non-functionalized high-performance pigment perinone in nothing but superheated water.[17] Since commercially available titanium alkoxides are prone to fast hydrolysis and aromatic compounds with carboxylic acid functionalities may suffer from decarboxylation in water at high temperature,[18] we decided to carry out reactions under solvothermal conditions using isopropanol ($^i$PrOH) as reaction medium. To our knowledge, the one-pot synthesis of organic pigment@$TiO_2$ HMs from molecular precursors has not been reported yet, neither solvothermally nor by other methods. However, there is a variety of different HMs synthesized via nonaqueous sol–gel processes from titanium alkoxides in the presence of carboxylato ligands in nonaqueous media, most prominently metal-organic frameworks (MOFs), e.g., MIL-125[19] or MOF-901,[20] and carboxylate stabilized titanium-oxo-clusters.[21] In addition, the use of titanium alkoxides as inorganic precursor molecules does theoretically not only grant access to the different bulk modifications of $TiO_2$, brookite, anatase, and rutile,[22] but also to a variety of mesoporous[23] and layered materials.[24] These materials find application in photocatalysis,[25] in wastewater purification,[26] as catalyst support,[27] or in lithium and post-lithium battery technologies.[28,29]

## 2. Results and Discussion

### 2.1. Solvothermal Synthesis and Characterization of the Perinonedicarboxylic Acid Pigment

Prior to the synthesis of the perinone@$TiO_2$ HMs, we needed to verify if the desired pigment perinonedicarboxylic acid (PDCA, **Scheme 1**) could be synthesized under solvothermal conditions using $^i$PrOH as the medium. These conditions were chosen, as $TiO_2$ can be readily synthesized from $Ti(O^iPr)_4$ (TTIP) in $^i$PrOH as solvent,[30] and as the development of a one-pot synthesis would require both a common solvent and common reaction conditions (e.g., *T*, *t*, etc.). Our literature survey disclosed a patented synthesis of PDCA, which is carried out in NMP or DMF at $T = 145$ °C and requires $Zn(OAc)_2$ as catalyst at reaction times of several hours.[31] The solvothermal synthesis of PDCA is not known in literature. As illustrated in Scheme 1, six isomers of PDCA are conceivable, namely three *cis*-isomers and three *trans*-isomers. Furthermore, it is expected that one obtains mixtures of these isomers, as mixtures of the *cis*- and the *trans*-isomer are also conventionally obtained for unsubstituted perinone.[32] To synthesize PDCA, the pigment precursors 3,4-diaminobenzoic acid (DABA) and naphthalene dianhydride (NDA) were suspended in 10 mL of $^i$PrOH and enclosed in a polytetrafluoroethylene (PTFE)-lined stainless-steel autoclave. The autoclave was placed in a heating block and was heated to the reaction temperature ($T_R$) of 180 °C for a reaction time ($t_R$) of 16 h. Then, the autoclave was allowed to cool down to room temperature in air, i.e., without additional cooling, which took ≈1.5 h

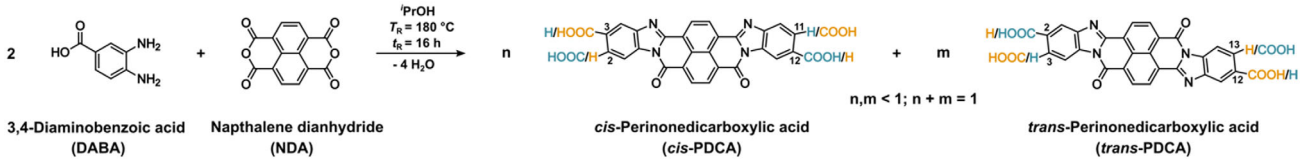


**Scheme 1.** Reaction scheme of the synthesis of the carboxylic-acid-functionalized perinone pigment PDCA. Naphthalene dianhydride (NDA) is reacted with two equivalents of 3,4-diaminobenzoic acid (DABA) to provide a potential mixture of six possible isomers of PDCA. The six isomers are *cis*-perinone-3,11-dicarboxylic acid, *cis*-perinone-2,12-dicarboxylic acid, *cis*-perinone-3,12-dicarboxylic acid, *trans*-perinone-2,12-dicarboxylic acid, *trans*-perinone-2,13-dicarboxylic acid, and *trans*-perinone-3,12-dicarboxylic acid.

(see Supporting Information for further details). A dark red suspension was obtained whose color significantly differs from those of the starting compounds, i.e., yellow (NDA) and brown (DABA), respectively. This is already indicative for the successful formation of the perinone core, as parent perinone without the $CO_2H$ group is a red pigment. Subsequently, the product was obtained as red powder through isolation by centrifugation, subsequent washing with $^{i}$PrOH and drying.

The attenuated-total-reflection Fourier transformation infrared (ATR–FTIR) spectrum (**Figure 1**A) of the product shows modes characteristic of the structural features of PDCA: 1) the carbonyl vibration at $\nu$(C═O) = 1700 (vs) cm $^{-1}$,[17] 2) the benzimidazole ring vibrations at $\nu$(C═N/C═C) = 1450 (m), 1380 (s), and 1355 (s) cm $^{-1}$,[17] and 3) the carboxylic acid carbonyl vibration as shoulder peak at $\nu$(C═O) = 1740 (m) cm $^{-1}$. Furthermore, PDCA features broad yet somewhat defined vibrational bands in the range of $\nu$ = 2500–3300 cm $^{-1}$ corresponding to $CO_2H^{\cdots}CO_2H$ (carboxylic acid) hydrogen bonding, between adjacent PDCA molecules. Interestingly, the precursor DABA exhibits significantly different hydrogen bonding features in this range (Figure 1A), which we attribute to $CO_2H^{\cdots}NH_2$ (or $CO_2^{-}{}^{\cdots}NH_3^{+}$) H-bonding of pure DABA in the solid state.[33] Furthermore, the ATR–FTIR spectrum of the isomeric mixture of PDCAs does neither show the carbonyl vibration of NDA ($\nu$(C═O) = 1765 (s) cm $^{-1}$)[17] nor the amine vibrations of DABA ($\nu(NH_2)_{as}$ = 3210 (m) cm $^{-1}$, $\nu(NH_2)_s$ = 3330 (m) cm $^{-1}$).[34] Next, PDCA was analyzed by

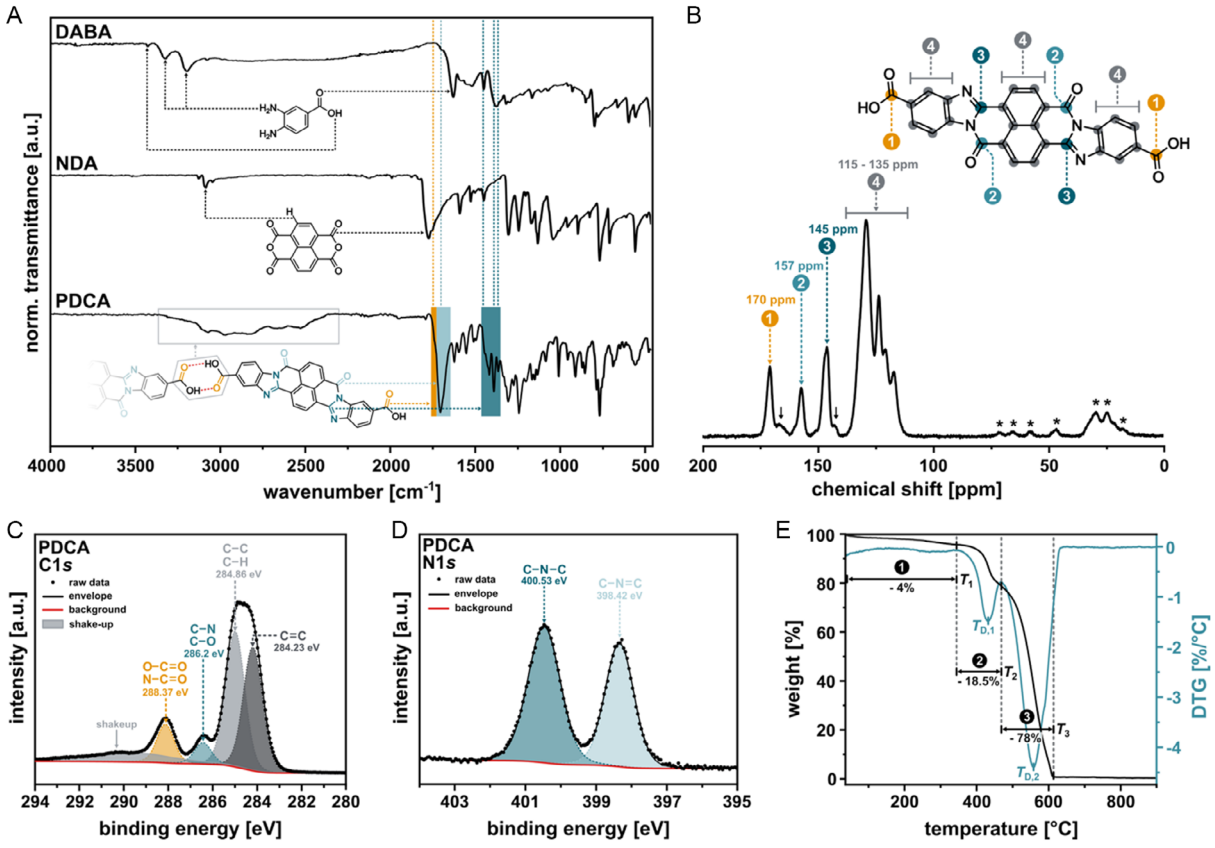


**Figure 1.** A) ATR–FTIR spectra of NDA, DABA, and PDCA. Modes relevant to chemical structure analysis are highlighted. B) $^{13}$C CP/MAS ss-NMR spectrum of PDCA with peak assignment. Rotational sidebands are marked by asterisks. Presumed byproduct signals are marked by black arrows. XPS spectra of PDCA of C) the C1s and D) N1s core signals. E) TGA curve of PDCA under $O_2$ atmosphere (black) and derivative of the TGA curve (DTG, petrol).

solid-state $^{13}C$ cross-polarization magic angle spinning nuclear magnetic resonance (ss-$^{13}C$ CP/MAS NMR) spectroscopy. The ss-$^{13}C$ CP/MAS NMR spectrum of PDCA (Figure 1B) features two signals that can be assigned to the carbonyl carbon atom **1** of the carboxylic acid with a chemical shift of $\delta = 170$ ppm and to the amide carbonyl **2** at $\delta = 157$ ppm. The signal at $\delta = 145$ ppm is assigned to the carbon atom **3**, i.e., the amidine carbon atom of the benzimidazole ring. The broad region from $\delta = 115$ ppm to $\delta = 135$ ppm is assigned to the carbon atoms of both the benzene and the naphthalene ring systems. Two shoulder peaks indicated by solid black arrows can either be associated with anisotropic peak broadening, the presence of different isomers, or, with low amounts of side products. We speculate that similar to the hydrothermal synthesis of perinone and other similar derived benzimidazoles, either partially unreacted NDA, naphthalene diimide, or benzimidazole species might be present in the product mixture.[17,35] X-ray photoelectron spectroscopy (XPS) measurements of the PDCA pigment (Figure 1C,D; full spectrum see Figure S1, Supporting Information) evince the presence of nitrogen, carbon, and oxygen by the appearance of characteristic signals of the C1*s*, O1*s*, and N1*s* core levels. Deconvolution of the C1*s* signal (Figure 1C) leads to a series of four peaks at 284.23, 284.86, 286.20, and 288.37 eV, which are assigned to C═C, C—C/C—H, C—N/C—O, and O—C═O/N—C═O bonds, respectively. The peaks associated with the C—O and O—C═O bonds indicate the presence of free carboxylic acid moieties in the PDCA pigment. Furthermore, deconvolution of the N1*s* signal (Figure 1D) shows two well defined peaks at 398.42 and 400.53 eV, which are assigned to C—N═C/C—N═O bonds and C—N—C bonds and indicate successful formation of the imidazole ring of the perinone core. Quantification of the elemental composition by XPS matches well with the theoretically calculated values for PDCA (77.8 at% carbon [calc. 73.6 at%], 8.2 at% nitrogen [calc. 8.3 at%], and 13.9 at% oxygen [calc. 12.5 at%]). We assume that the slight deviation of the theoretical carbon and oxygen contents can be attributed to contamination of the samples by adventitious carbon, residual reaction solvent $^{i}$PrOH (presence indicated by thermogravimetric analysis, TGA, as discussed subsequently), or the possible presence of side products derived from the NDA precursor as pointed at by ss-$^{13}C$ CP/MAS NMR.

Furthermore, we performed TGA of PDCA in $O_2$ atmosphere (Figure 1E). An initial weight loss of 4 wt% from room temperature to 200 °C was assigned to physisorbed small molecules. We suppose that these are mainly the solvent of the solvothermal synthesis ($^{i}$PrOH, $T_{vap} = 82$ °C) as well as adsorbed humidity ($H_2O$, $T_{vap} = 100$ °C) from the ambient atmosphere.

A second weight loss of 18.5 wt% from $T_1 = 350$ °C until $T_2 = 470$ °C and a first decomposition temperature ($T_{D,1}$) of 428 °C are assigned to the decarboxylation of the carboxylic acid groups, as the theoretical mass contribution of two carbon dioxide molecules to the PDCA molecule is 17.5 wt%. We assume that upon heating in $O_2$ atmosphere, PDCA fully decarboxylates between 350 and 470 °C. A third mass loss step starts at $T_2 = 470$ °C. This mass loss of overall 78 wt% is completed at $\approx T_3 = 611$ °C and is attributed to the full decomposition (i.e., degradation into $CO_2$, CO, $H_2O$, and $NO_x$) of the remaining perinone core (decomposition temperature $T_{D,2} = 558$ °C, determined by differential method).

Next, we analyzed the order of PDCA by powder X-ray diffraction (PXRD) measurements. The diffractogram of PDCA (**Figure 2**A) shows no amorphous background but several reflections. These are found at $2\theta(Cu–K_\alpha) = 11°$, 13°, 25°, and 27°, which clearly differ from those of the starting compounds. It becomes clear that the starting compounds show diffraction patterns that are different from that of PDCA (Figure 2A). Note that compared to NDA and DABA, the reflections of PDCA are significantly broader, which we attribute to significant orientational and positional disorder. Parent perinone is well known for forming solid solutions of the *cis*- and *trans*-isomer in virtually any ratio, as the structure can accommodate large amounts of "defects" in the form of positional and orientational disorder.[32,36]

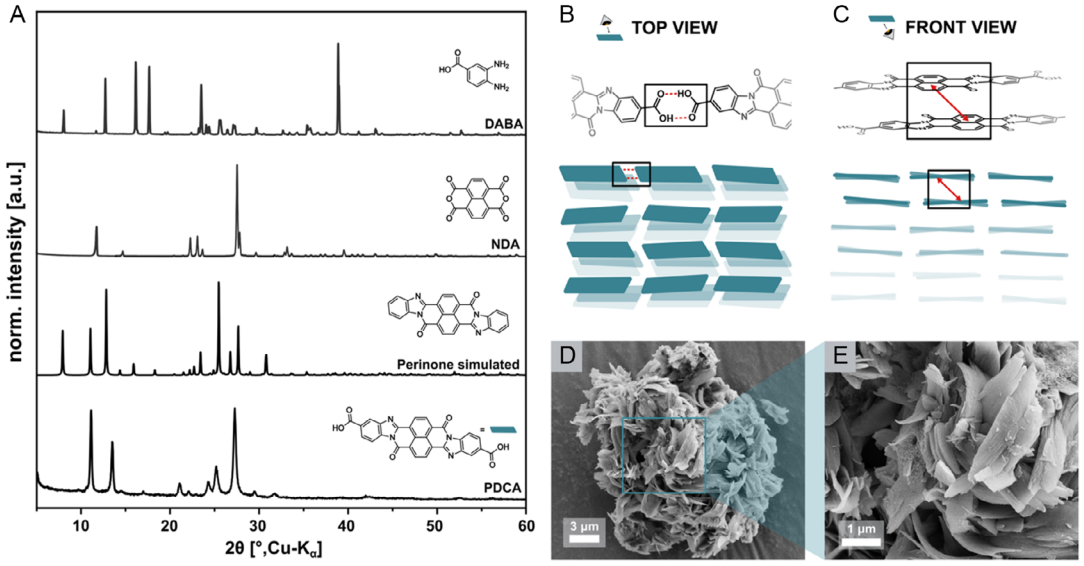


**Figure 2.** A) PXRD of NDA, DABA, and the PDCA pigment. B,C) Schematic illustration of the possible arrangement of PDCA molecules in the solid state, resembling liquid-crystalline-alike phases. D,E) SEM images of the PDCA pigment.

Therefrom and from the observed strong H-bonding modes in the ATR–FTIR spectrum of PDCA (see Figure 1A), we conclude the presence of H-bonded PDCA molecules that potentially arrange into phases featuring infinite π stacks with significant positional and orientational disorder, corresponding to liquid-crystalline-alike phases (as illustrated in Figure 2B,C).[37]

Scanning electron microscopy (SEM) images (Figure 2D,E) evince that the PDCA pigment forms aggregates of ≈15 μm in diameter. These are composed of ribbons that are ≈3–5 μm long and ≈1 μm wide at ≈100 nm thickness. Most interestingly, they are strongly bent. Bending in small molecule crystals has often been associated with the presence of significant amounts of mobile noncovalent intermolecular interactions.[38] Consequently, the observed morphologies appear to be in line with the significant H-bonding modes in the ATR–FTIR spectrum of PDCA (Figure 1A).

Overall, we conclude that the carboxylic acid functionalized perinone pigment PDCA can be synthesized in neat $^{i}$PrOH under solvothermal conditions ($T_R = 180$ °C, $t_R = 16$ h).

### 2.2. One-Pot Synthesis and Characterization of the PDCA@$TiO_2$ HM Exhibiting Lepidocrocite-Like Structure

To achieve the simultaneous synthesis of $TiO_2$ and PDCA and, possibly an HM derived from them in a one-pot synthesis, a modified sol–gel process was applied using $Ti(O^{i}Pr)_4$ as precursor. Titanium alkoxides are significantly more reactive toward hydrolysis than silicon alkoxides due to the higher bond polarity ($\Delta EN(Ti{-}O) = 1.90$ vs $\Delta EN(Si{-}O) = 1.54$). Therefore, a large excess of $H_2O$, which is for instance the case when $H_2O$ is used as solvent, leads to the immediate formation of $TiO_2$. Hence, a hydrothermal one-pot pigment@$TiO_2$ synthesis is likely impossible to achieve in a solvent system containing substantial quantities of water, as the pigment cannot be generated within the very short timeframe of complete $TiO_2$ formation. However, to allow for the controlled hydrolysis of TTIP and subsequent condensation to $TiO_2$, a small amount of $H_2O$ is required. The ideal stoichiometry would be 1:4 (Ti:$H_2O$), yet typically slightly larger Ti:$H_2O$ ratios of 1:6–1:20 are usually employed for controlled hydrolysis.[39] We hypothesized that the four equivalents of $H_2O$ molecules formed by the formation of PDCA from condensation of NDA with two molecules of DABA could be an optimal source of $H_2O$ for the controlled hydrolysis of TTIP. Furthermore, we hypothesized that PDCA's $CO_2H$ groups might allow for covalently linking the pigment to the $TiO_2$ component. Overall, we attempted the one-pot synthesis of a perinone@$TiO_2$ HM with covalent linking of organic and inorganic components directly from the precursors TTIP, DABA, and NDA (**Figure 3**A). As our attempt to synthesize the pigment PDCA solvothermally in $^{i}$PrOH was successful and it is well known that $TiO_2$ can be synthesized under solvothermal conditions,[30,40] we hypothesized that these conditions might allow for generating an actual class II HM of the two components. Specifically, the synthesis consisted of suspending the PDCA precursors DABA and NDA in 10 mL of $^{i}$PrOH and adding TTIP rapidly. As for the previously described synthesis of PDCA itself, the mixture was transferred to a PTFE-lined autoclave and placed in a heating block (see Supporting Information). The autoclave was heated to $T_R = 180$ °C for $t_R = 16$ h. After $t_R$, the autoclave was allowed to cool down to room temperature at air. A red suspension was obtained, and the product was isolated via centrifugation. The product obtained is, as we will show in the following, a layered lepidocrocite-type class II HM. To the best of our knowledge, this is the first $TiO_2$-class II HM obtained by simultaneous synthesis and linking of both an organic pigment and an inorganic $TiO_2$ compound.

The ATR–FTIR spectrum of PDCA@$TiO_2$ (Figure 3B) shows the characteristic carbonyl mode of PDCA at $\nu(C{=}O)_s = 1700$ (vs) cm$^{-1}$ and its benzimidazole vibrations at $\nu(C{=}N/C{=}C) = 1355$ (m), 1380 (m), and 1450 (m) cm$^{-1}$. These modes are identical with those of the PDCA pigment prepared for reference (see Figure 1A). Furthermore, compared to PDCA, in the HM, the carboxylic acid H-bonding modes at $\nu = 2500$–$3300$ cm$^{-1}$ are absent while carboxylate modes are present at $\nu(COO)_s =$ 1410 (m) cm$^{-1}$ and $\nu(COO)_{as} = 1540$ (m) cm$^{-1}$. This indicates the transformation of $-CO_2H$ to $-CO_2$ and its coordination to $Ti^{4+}$ centers as carboxylato ligand. Moreover, no amine vibrations of the starting compound DABA are present in the HM, evincing that no remains of the starting compound DABA are present in the HM. The presence of Ti–O bonds in the HM is indicated by the presence of titanol surface hydroxy groups $\nu(Ti{-}OH) = 2750$–$3600$ (br) cm$^{-1}$ and titanium oxygen bonds $\nu(Ti{-}O{-}Ti) = 680$ (m) cm$^{-1}$. Furthermore, modes corresponding to aliphatic CH groups and ester groups are visible in the spectrum ($\nu(CH)_{as} = 2850$ (m) and $\nu(CH)_s = 2970$ (m) cm$^{-1}$, $\nu(C{-}O{-}C) = 1100$ (s) cm$^{-1}$), indicating the presence of either isopropoxide groups formed by side reactions, or residuals of $^{i}$PrOH, or both, within the PDCA@$TiO_2$ product. Next, ss-$^{13}$C CP/MAS NMR spectroscopy, in line with ATR–FTIR spectroscopy, confirms the successful synthesis of the perinone core (Figure 2C): the carbonyl carbon atom **2** is assigned to the peak at $\delta = 157$ ppm, and the benzimidazole carbon **3** is found at $\delta = 145$ ppm. The broad peaks at $\delta = 110$–$153$ ppm are assigned to the benzene and naphthalene aromatic carbon atoms. Successful bonding of the carboxylic acid to Ti centers is indicated by the absence of the peak associated with the carbonyl carbon atom of the free carboxylic acid of PDCA at $\delta = 170$ ppm. Instead, a peak at $\delta = 174$ ppm is assigned to the carbonyl **1** of the carboxylate connected to the Ti centers in bridging fashion. Signals at $\delta = 163$, 69, and 25 ppm (indicated by black arrows), which correspond to carbon atoms of ester and methyl groups, confirm the presence of isopropyl ester byproducts in the HM, which were already indicated by ATR–FTIR.

Interestingly, the signals associated with ester byproducts are absent in the ATR–FTIR and ss–$^{13}$C CP/MAS NMR spectra of the PDCA pigment alone generated solvothermally (cf. Figure 1A,B). Therefore, we speculate that the ester byproducts' formation is mediated by TTIP, which promotes the condensation of $^{i}$PrOH with DABA or NDA, and/or via the transesterification of coordinated isopropoxide groups with Ti-coordinated DABA or NDA. XPS analysis of the PDCA@$TiO_2$ HM reveals the presence of nitrogen, carbon, oxygen, and titanium by the appearance of signals of the N1*s*, C1*s*, O1*s*, and Ti2*p* core levels. Like for PDCA (cf. Figure 1C), deconvolution of the C1*s* signals (Figure 2A) leads to a series of peaks at 284.23, 284.86, 286.20, and 288.37 eV, indicating the presence of C=C, C–C/C–H, C–O/C–N, and O–C=O/N–C=O bonds. In direct analogy to

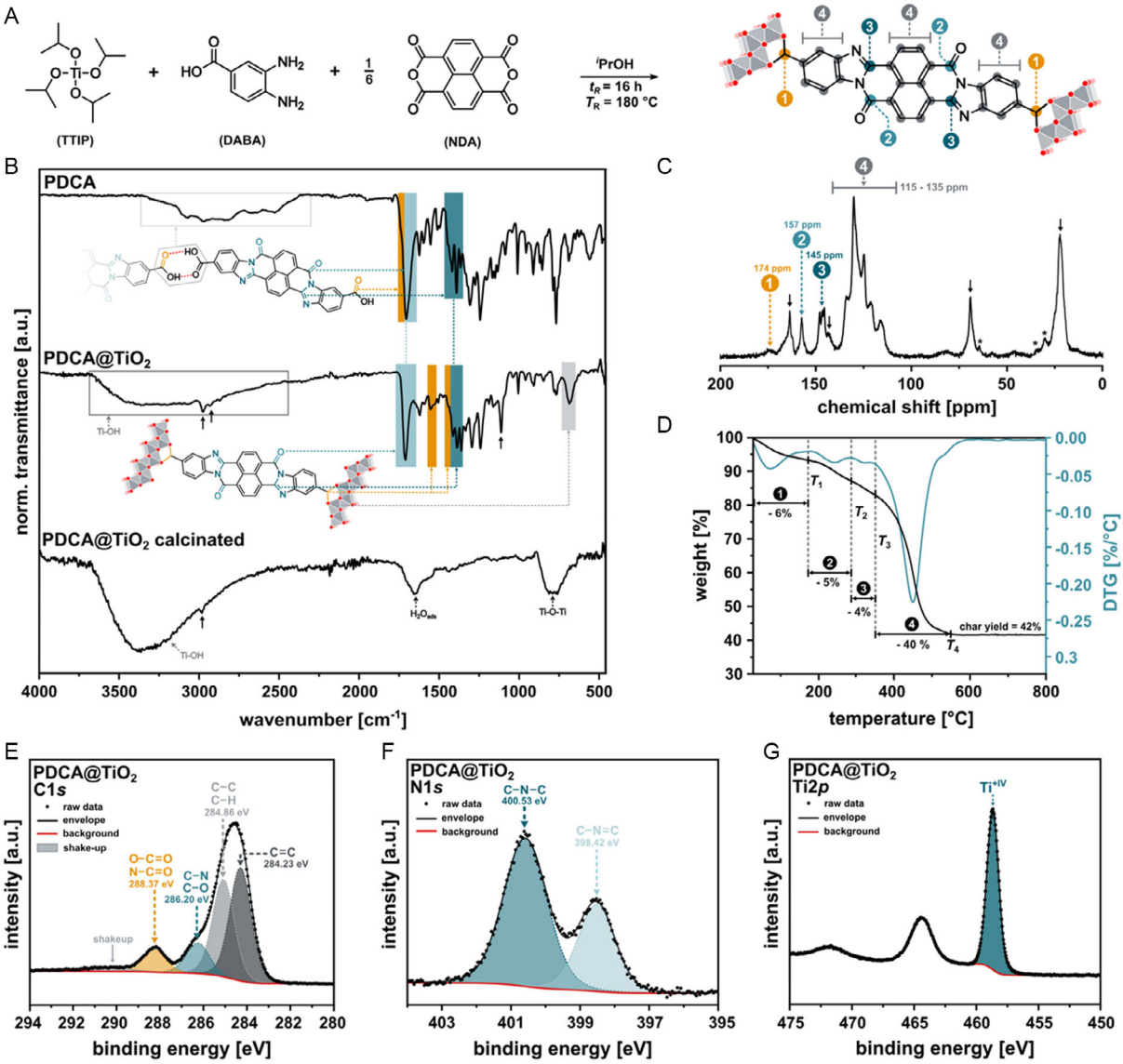


**Figure 3.** A) Reaction scheme of the synthesis of the PDCA@$TiO_2$ HM. B) ATR–FTIR spectra of PDCA, the PDCA@$TiO_2$ HM, and the HM calcinated at 600 °C for 3 h. C) ss-$^{13}$C CP/MAS NMR spectrum of the PDCA@$TiO_2$ HM with peak assignment in the product depicted in (A). Rotational sidebands are marked by asterisks. Byproduct signals are indicated by arrows. D) TGA of the PDCA@$TiO_2$ HM under $O_2$ atmosphere: TGA curve (black) and derivative of the TGA curve (DTG, petrol). High-resolution XPS spectra of PDCA@$TiO_2$ showing E) C1*s*, F) N1*s*, and G) Ti2*p* core signals.

the PDCA pigment, the PDCA@$TiO_2$ HM gives a higher intensity signal of the C—O/C—N bonds relative to the O—C=O bond signal. This can be attributed to an increased amount of C—O—C bonds and consolidates the hypothesis of ester byproducts formed by side reactions as indicated by ATR–FTIR and $^{13}$C ss-NMR. Byproduct formation presumably also leads to different intensity contributions of the two distinct N1*s* core-level signals (Figure 2F). Here, the signal attributed to the C—N=C bond at 398.42 eV is less intense than the C—N—C signal at 400.43 eV. This cannot be explained solely by ester byproduct formation and we assume that byproducts form in a similar fashion to observations by Mamada et al. in the reaction of aromatic anhydrides with diamines using $Zn(OAc)_2$ as Lewis acid catalyst and employing an excess of either of the starting compounds (as illustrated in Figure S2, Supporting Information).[35] The single Ti2*p* core-level signal (Figure 2G) at 458.62 eV implies that the titanium atoms in the PDCA@$TiO_2$ HM are in oxidation state +IV. TGA of the HM (Figure 2D) shows a first gradual weight loss of 6 wt% up to a temperature $T_1$ of 130 °C, which we attribute to physisorbed small molecules (residual $^i$PrOH; adsorbed $H_2O$ from air humidity). Next, a step with a weight loss of 5 wt% from $T_1 = 130$ °C until $T_2 = 270$ °C is attributed to the release of $H_2O$ upon the condensation of titanol groups, in accordance to the literature.[41] Next, a step with a weight loss of 4 wt% at an onset temperature of $T_2 = 270$ °C until $T_3 = 350$ °C is identified. We attribute this step to the decomposition of the side products that

$^{13}$C ss-NMR, ATR–FTIR, and XPS spectra strongly indicated. Finally, a weight loss of 40 wt% from $T_3 = 350\,°C$ until $T_4 = 550\,°C$ corresponds to the decomposition of the perinone functionality. The absence of aggregates of PDCA molecules with a high degree of π–π stacking most likely leads to the lower onset temperature of the decomposition of the perinone functionality (350 °C for PDCA@$TiO_2$ vs 400 °C for PDCA). In addition, from the TGA curve, a residual mass of 42 wt% at $T_4 > 550\,°C$ is attributed to the remaining inorganic $TiO_2$. From the last step accounted to the decomposition of PDCA ($T_3$ to $T_4$) and the observed residual mass, a ratio of Ti:PDCA of 6.7:1 was determined. Considering the starting compound stoichiometry supplied in the synthesis (6:1 of Ti:NDA), this corresponds to an overall conversion of NDA of 90%. Consequently, we conclude that ≈10% of NDA were converted to the postulated side products.

Structural analysis of the HM by PXRD (**Figure 4**A) evinces order. Reflections around $2\theta(Cu–K_\alpha) = 4.8°$, 11.0°, 23°–28°, and 48.8° fit very well the with a layered lepidocrocite-like $TiO_2$ structure.[42–44] Lepidocrocite-like titanates are structures composed of layers of edge-sharing [$TiO_6$] octahedra. Typically, they contain $H^+$ or alkali metal counterions in between the layers to balance the negative charges that arise in layers of edge-sharing octahedra. Such structures are known and named after the iron

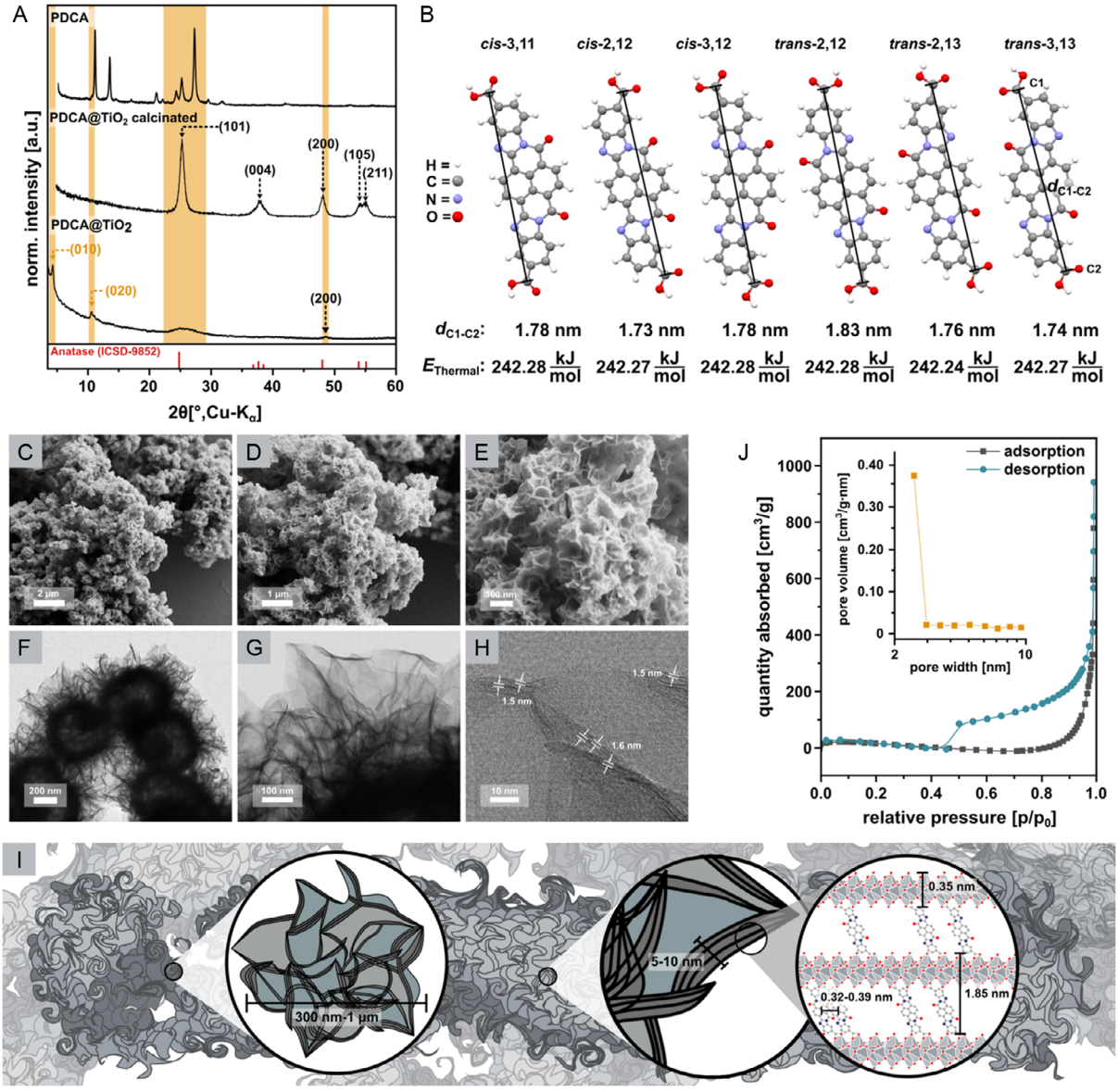


**Figure 4.** A) Diffractograms of PDCA and the calcinated (range: $2\theta = 5°–60°$) and as-synthesized PDCA@$TiO_2$ HM (range: $2\theta = 2°–60°$) and simulation of anatase $TiO_2$ (ICSD-9852 [ICSD release 2013.1][53,54]). B) DFT calculated and optimized structures of different isomers of the PDCA pigment with their thermal energies. C–E) SEM images of the PDCA@$TiO_2$ HM. F–H) HRTEM images of the PDCA@$TiO_2$ HM. I) Schematic representation of the hierarchical structure of the PDCA@$TiO_2$ HM. J) $N_2$ physisorption measurement of the PDCA@$TiO_2$ HM: adsorption–desorption isotherm and BJH pore size distribution (inset, orange).

oxide hydroxide mineral lepidocrocite (γ–FeO(OH)), as pure $TiO_2$ does not express such structures. Instead of exclusively edge-sharing octahedra, all thermodynamically stable $TiO_2$ polymorphs, i.e., anatase, brookite, and rutile, are featuring both edge- and corner-sharing octahedra (anatase, brookite) or solely corner-sharing octahedra (rutile). According to a lepidocrocite-like structure, the reflections are indexed as $2\theta(Cu{-}K_\alpha) = 4.8$ (010), 11.0° (020), 23° (110) to 28° (130), and 48.8° (200) (Figure 4A). From applying Bragg's law to the (010) reflection $2\theta(Cu{-}K_\alpha) = 4.8°$, a $d$ spacing of two adjacent lepidocrocite-like layers of $d_{010} = 1.85$ nm results. Considering that the $[TiO_6]$ layers themselves have a thickness of 0.35 nm, an interlayer spacing of 1.50 nm results from the top of one layer to the bottom of the next upper layer. This distance is attributed to organic spacers in between sheets. We have quantum-chemically calculated and optimized the structures of all possible PDCA isomers (Figure 4B, see Supporting Information for computational details), which gives lengths of 1.7–1.8 nm. Note that the DFT calculations yield very similar thermal energy values for the respective isomers of 242.2–242.3 kcal mol$^{-1}$. This translates to none of the isomers being energetically favored over the others and hence points at a high likelihood for any PDCA synthesis to yield a nearly statistical mixture of isomers. As the HM's diffractogram fits a lepidocrocite-type structure with an interlayer spacing of ≈1.5 nm, we conclude that the edge-connected $[TiO_6]$ octahedral sheets are spaced by inclined pigment molecules. From the interlayer distance being ≈20% shorter than the pigment molecules' length, we expect the pigment molecules to be tilted in a ≈35° angle with respect to the inorganic layers (see Figure S3, Supporting Information). Tilted organic spacers have been postulated in structurally similar class I HMs like dopamine/$MoS_2$[45] and *L*-dopamine/lepidocrocite-like $TiO_2$.[46] In addition, class I lepidocrocite-like HMs featuring aliphatic amines such as *n*-octylamine intercalated into titanates have been reported.[47] Usually, the negative charge of the titanate layers is compensated via cation exchange or intercalation of the respective organic molecule.[47] All these materials are, in contrast to the here presented HM, class I HMs, with H-bonding/electrostatic interactions between cationic ammonium $NH_3^+$ and anionic $S^\delta$ /$O^\delta$ atoms of $MoS_2/TiO_2$ layers, respectively. Notably, layered materials with nonaromatic, aliphatic spacers do not feature the broad reflection in the range of $2\theta(Cu{-}K_\alpha)$ ≈23°–28° but a single reflection at $2\theta(Cu{-}K_\alpha)$ ≈26°, which corresponds to the thickness of the inorganic layers. We conjecture that the broad reflection arises from a distribution of π–π-stacking PDCA molecules with different spacing in between the sheets overlapping with the reflection associated with the inorganic layer thickness as the center of the broad reflection is at ≈26°, which also corresponds to an ideal π–π stack with distances of $d_{\pi-\pi} = 0.35$ nm in between two adjacent molecules of PDCA. This would imply that 1) PDCA–PDCA π-stacked dimers exist in the HM's structure, and 2) that some of these dimers are relatively close to each other ($d_{\pi-\pi}$ [29°] ≈ 0.32 nm). The latter is conceivable considering offset π–π stacks at <40° inclination angles. For further clarifying the composition, the HM was calcinated at $T_C = 450$ °C for $t_c = 3$ h under air flow. Per the previously discussed TGA analysis of PDCA@$TiO_2$, this temperature should be sufficient for fully removing the pigment component by degradation to CO, $CO_2$, $H_2O$, and $NO_x$. By this treatment, the HM was converted to anatase $TiO_2$, as indicated by the appearance of characteristic reflections at $2\theta(Cu{-}K_\alpha) = 25°$ (101), 37° (004), 48° (200), 54° (105), and 55° (211) (Figure 4A). Note that the breadth of the anatase reflections is a consequence of their nanoscopic particle sizes. Furthermore, the ATR–FTIR spectrum corresponds well to $TiO_2$ (with titanium–oxygen vibrations at $\nu$(Ti–O–Ti) = 610–880 (m) cm$^{-1}$) that is to some degree hydroxylated and hydrated ($\nu$(Ti—OH) = 2750–3600 (br) cm$^{-1}$ and surface adsorbed water at $\nu = 1620$ cm$^{-1}$, see Figure 3B). The fact that $TiO_2$ results from the calcination hints at $[TiO_X]$ already being present in the pristine HM, hence supporting the hypothesis of the successful formation of a PDCA@$TiO_2$ HM further.

SEM imaging reveals spongelike spherical aggregates featuring pores of ≈200 nm in diameter and sheetlike cell walls of <50 nm in thickness. Furthermore, SEM imaging after calcination (see Figure S4, Supporting Information) confirms the transformation of the uniform spherical spongelike morphology of the HM to dense micron-sized aggregates of nanoparticles (NPs) upon calcination. Given that, from TGA, the PDCA component is decomposing upon calcination, it seems plausible that the structure collapses to dense NP aggregates, as observed for other titanates.[48,49]

Next, we investigated the PDCA@$TiO_2$ HM by high-resolution transmission electron microscopy (HRTEM) and the resulting images are displayed in Figure 4F–H. From HRTEM, it becomes clear that the spherical spongelike aggregates are composed of nanosheets. The layered structure can be observed in the HRTEM images as alternating lines of different contrast (see Figure 4H). Areas containing the inorganic component, here $[TiO_6]$ layers, result in a higher contrast, while areas containing purely organic components, here PDCA, give lower contrast. From HRTEM, the measured $d$ spacing between the inorganic layers at different positions varies between 1.4 and 1.6 nm (Figure 4H). This is consistent with the interlayer distance determined from PXRD (Figure 4A). From all chemical (ATR–FTIR, ss-$^{13}$C CP/MAS NMR), structural (PXRD, DFT calculations, HRTEM) and morphological (SEM, HRTEM) analyses performed, we conclude that PDCA@$TiO_2$ is a lepidocrocite-like layered class II HM composed of $[TiO_6]$-edge-sharing layers bridged by PDCA molecules. This corresponds to a structure as schematically depicted in Figure 4I (right) with a channel structure between $[TiO_6]$ layers and PDCA molecules. From these channels and the spongelike morphologies, featuring cell diameters of 30–50 nm from HRTEM and SEM images, porosity, and a relatively high Brunauer–Emmett–Teller (BET) surface area are expected. To verify this hypothesis, we performed $N_2$ physisorption measurements (see Figure 4J). The PDCA@$TiO_2$ HM shows no accessible microporosity (<2 nm), indicated by the absence of significant adsorption of $N_2$ below a relative pressure of $p/p_0 = 0.1$.[50] At relative pressure values of $p/p_0 = 0.4$–1, a type IV adsorption–desorption isotherm is identified, indicating the presence of mesopores in the HM. The adsorption–desorption isotherm in this relative pressure range shows an H3 hysteresis that is based on capillary condensation of $N_2$ within the mesopores of the material. From this, and in agreement with the literature,[50] the presence of slit-like pores within the material is concluded. The extracted Barrett–Joyner–Halenda (BJH) pore size distribution confirms the presence of mesopores with a

maximum at a pore width of 3.3 nm (Figure 4J, inset). The mesoporosity leads to a specific BET surface area of 127.4 $m^2 g^{-1}$.

### 2.3. Expansion of the One-Pot Pigment@$TiO_2$ HM Synthesis to Other Benzimidazole-Type Pigments

Since the synthesis of the class II perinone@$TiO_2$ HM was successful, we were intrigued to check if such lepidocrocite-like pigment@$TiO_2$ HMs employing small molecules other than perinone would be generally achievable by the here presented one-pot synthesis. It should in theory be possible to incorporate a variety of different spacers in between lepidocrocite-like [$TiO_6$] layers. As aromatic, aliphatic, and semiaromatic dianhydrides are standard monomers for the synthesis of cyclocondensation polymers (mainly polyimides), they are commercially available in great variety. Consequently, we chose to capitalize upon this accessible variety and substitute the NDA component of the PDCA synthesis by benzophenone tetracarboxylic dianhydride (BTDA), pyromellitic dianhydride (PMDA), and bisphenol A dianhydride (BPADA), respectively. We expected the use of these different linker molecules to go along with a corresponding change in the *d* spacing of the inorganic [$TiO_6$] layers. PXRD measurements of the HMs with different linkers (**Figure 5**A) confirm the successful formation of the lepidocrocite-like structure by the low-intensity characteristic reflections at $2\theta(Cu–K_\alpha) =$ 23°–28° and 48°. In addition, reflections at lower angles are visible for all dianhydrides at $2\theta(Cu—K_\alpha) = 2.25°$ (PMDA), 2.42° (BPADA), and 2.95° (BTDA). Due to these reflections, the formation of a similar layered structure as the PDCA@$TiO_2$ HM with different *d* spacings can be concluded. Consequently, from applying Bragg's law, *d*-spacing values of $d_{010} = 3.9$ nm (PMDA), $d_{010} = 3.7$ nm (BPADA), and $d_{010} = 3.0$ nm (BTDA) result. We attribute the change in *d* spacing in the case of BPADA and BPTA-based HMs to 1) the difference in size of the linker molecules themselves and 2) differences in the intermolecular interactions of the aromatic core units. BPADA and BPTDA both contain bridges in between benzene rings (—$C(CH_3)_2$— and C═O, respectively) that interrupt the planarity and π conjugation of the pigment component and therefore will engender less efficient π–π stacking in comparison to the fully π–conjugated PDCA. This results in increased *d* spacings. In contrast, the shortest employed anhydride-derived (PMDA) pigment@$TiO_2$ features the biggest *d* spacing. We assume that the larger interlayer distance results from, partial attachment of the carboxylic acid moieties to only one [$TiO_6$] layer, which results in a lamellar stacked structure similar to *n*-alkylamine-intercalated lepidocrocite-like titanates. For all HMs derived from different dianhydrides, SEM imaging evinces morphologies very similar to PDCA@$TiO_2$: all three HMs are composed exclusively of aggregates of spongelike particles from ≈300 nm to 1 µm in diameter (Figure 5B–E).

### 2.4. Electrochemical Tests of PDCA@$TiO_2$

The combination of organic component (perinone) with inorganic component ($TiO_2$) in a class II HM that features channel-like porosity seems composition- and structure-wise potentially interesting for energy applications. Indeed, there are several examples of applications of both lepidocrocite-like titanates and fully conjugated organic compounds in electrochemical applications.[29,46,51,52] In the case of PDCA@$TiO_2$, we hypothesize that the layered structure of the HM could be beneficial for ion intercalation. The electrochemical properties were hence evaluated in two-electrode Swagelok cells containing metallic lithium as counter electrode and compared to that of pure PDCA and a $TiO_2$ standard (P25). **Figure 6**A shows the first five charge and discharge galvanostatic cycling with potential limitation (GCPL) profiles of a cell containing the PDCA@$TiO_2$ hybrid structure at a 0.5 C rate between 1.5 and 3.5 V versus $Li/Li^+$. The cell delivered an initial discharge capacity of 123 mAh $g^{-1}$, of which 79 mAh $g^{-1}$ was recovered on the first charge. The comparatively low first cycle Coulombic efficiency

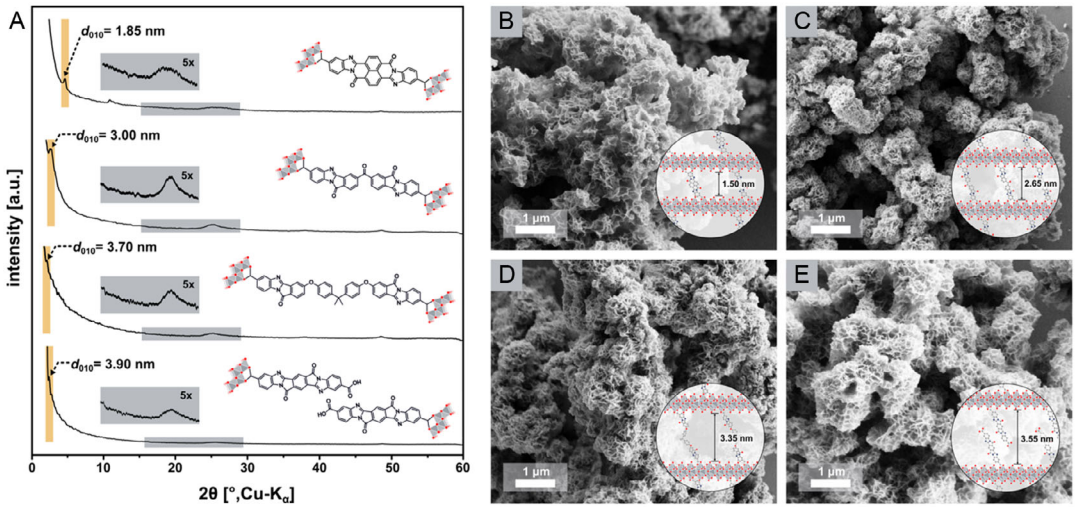


**Figure 5.** A) PXRD patterns of HMs with different linkers derived from different dianhydrides, namely benzophenone tetracarboxylic dianhydride (BTDA), bisphenol A dianhydride (BPADA), pyromellitic dianhydride (PMDA), and naphthalene dianhydride (NDA). SEM images of the HMs synthesized: B) NDA, C) BTDA, D) BPADA, and E) PMDA. Insets of (B)–(E): schematic illustration of the proposed layered structure of the HMs presented.

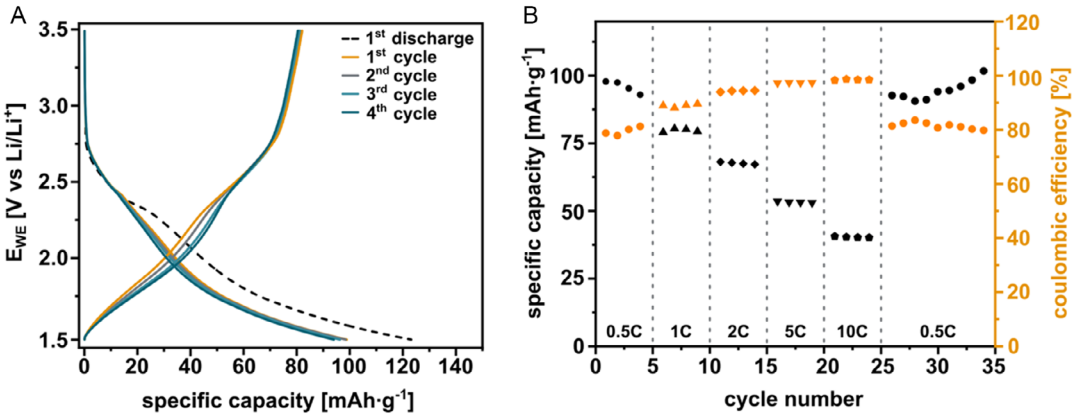


**Figure 6.** A) GCPL profiles of PDCA@$TiO_2$ at 0.5 C. B) Discharge capacity versus cycle number of the corresponding cell (black) and Coulombic efficiency (orange).

can be attributed to various side reactions at low potential, electrolyte decomposition, and probable solid electrolyte interphase formation. Interestingly, the voltage profiles of PDCA@$TiO_2$ upon initial cycling show that the HM is electrochemically active with first a pseudo plateau located at ≈2.4 V versus $Li/Li^+$ followed by two successive linear potential decays down to 1.5 V versus $Li/Li^+$. This profile is not observed for pure PDCA or $TiO_2$ (Figure S7A,C, Supporting Information). It is therefore assumed to result from the class II hybrid nature of the PDCA@$TiO_2$ material with modification of the energies of the redox centers when compared with the active materials tested separately. Indeed, the voltage profile of the pure PDCA-(organic) and $TiO_2$-(inorganic) based electrodes each exhibit a one-step reduction process with a potential plateau observed at ≈1.8 V versus $Li/Li^+$ for $TiO_2$ (Figure S7C, Supporting Information) and a linear potential decay between 2.8 and 1.9 V versus $Li/Li^+$ for PDCA (Figure S7A, Supporting Information). Figure 6B exhibits the rate capability of the PDCA@$TiO_2$ and Figure S7B,D, Supporting Information, of the pure PDCA and $TiO_2$, respectively. In all cases, significant improvement in terms of Coulombic efficiency is observed when increasing the C rate pointing at irreversible reduction processes (such as irreversible electrode or electrolyte reduction) being less kinetically favorable than $Li^+$ insertion. However, significant differences in the evolution of the Coulombic efficiency upon cycling and in terms of power performances can be observed between the HM and the pure separated components. For instance, the Coulombic efficiency recorded at 0.5 C for the pure PDCA is below 60% during the first few cycles but gradually increases to reach 98% at 10 C. By contrast, both $TiO_2$ and PDCA@$TiO_2$ present initial Coulombic efficiencies of about 80% (at 0.5 C) which quickly increase to ≈99% for C rates at or above 2 C. Pure $TiO_2$ presents the worst power performances with initial capacity at 0.5 C of about 150 mAh $g^{-1}$, which decreases to ≈50 mAh $g^{-1}$ at 5 C (i.e., 33% capacity retention). In contrast, pure PDCA and PDCA@$TiO_2$ retain about, respectively, 70% and 60% of their capacity between 0.5 and 5 C. Overall, the HM presents clear synergistic effects and possesses positive attributes of both individual pure components, i.e., good Coulombic efficiency of $TiO_2$ and power performances of the pure PDCA. Comparative impedance analysis of the PDCA@$TiO_2$ along with its inorganic and organic counterpart (Figure S8, Supporting Information) suggests slightly higher charge-transfer resistance in the HM, which may be attributed to the covalent linking of the PDCA pigment to the lepidocrocite-like $TiO_2$ and thus resulting in reduced electronic conductivity. This, however, does not significantly impact power performances since, as mentioned previously, the HM presents better rate capability than pure $TiO_2$, highlighting the fact that the rate-limiting step in these active materials is not related to charge transfer and electronic conductivity.

## 3. Conclusion

In this work, we presented the first pigment@$TiO_2$ class II HMs by simultaneous synthesis of both its organic and inorganic components in a one-pot solvothermal approach. The synthesis is simple and benign as nothing but the starting compounds $Ti(O^iPr)_4$, an organic dianhydride, DABA, and the non-harmful solvent $^i$PrOH are needed. To obtain covalently linked class II HMs, we first showed that the organic carboxylic acid bearing pigment PDCA can readily be synthesized under solvothermal conditions from its building blocks DABA and NDA. The composition of the PDCA pigment was determined by ATR–FTIR, ss-$^{13}$C CP/MAS NMR, TGA, and XPS analysis. Morphological analysis by SEM showed that PDCA exhibits a microflower-like morphology. After successful synthesis of PDCA, we aimed at combining the pigment building blocks NDA and DABA with TTIP in a modified sol–gel process. We hypothesized, that the water released by the slow reaction of NDA and DABA upon reaction to the PDCA pigment would provide a controlled hydrolysis of the titanium alkoxide precursor. The material obtained exhibits a layered lepidocrocite-like structure spaced by pigment molecules. Interlayer distances of 1.50–1.85 nm were determined by PXRD and HRTEM measurements. In addition, we show that the herein reported procedure to a whole new class of $TiO_2$-based type II HMs can be generalized. We thus synthesized three further HMs with similar structure by employing different organic linker molecules. With these different linkers, we observed different interlayer distances in between lepidocrocite-like layers.

We expect these new materials to pave the way for the design of new layered titanium class II hybrid nanomaterials with precisely tuned properties, which are desired for electrochemical and optoelectrical applications. Therefore, we decided to carry out proof-of-concept battery tests in lithium half-cells employing PDCA@$TiO_2$ as composite cathode. The PDCA@$TiO_2$ HM is electrochemically active and presents a clear synergistic effect with a Coulombic efficiency similar to pure $TiO_2$ (and much higher than pure PDCA) and a rate capability similar to PDCA (and much higher than $TiO_2$). Furthermore, the presence of large interlayer spacings in the HM might be expendable to the use of cations with larger ionic radii ($Na^+$, $K^+$) or with higher charge density ($Ca^{2+}$, $Mg^{2+}$), as diffusion might be promoted along the porous layers in between the organic moieties. This would presumably lead to a marked increase in Coulombic efficiency and better reversibility in the often diffusion-limited inter- and deintercalation processes of such cations.

## Supporting Information

Supporting Information is available from the Wiley Online Library or from the author.

## Acknowledgements

The authors acknowledge the Austrian Science Fund (FWF) for financial support under grant no. START Y1037-N28. The Austrian Research Promotion Agency (FFG) is gratefully acknowledged for funding of the XPS infrastructure (FFG project number: 884672). A.P. gratefully acknowledges funding from the European Research Council (ERC) under the European Union's Horizon 2020 research and innovation program (grant agreement no. 101089281) and the Spanish Agencia Estatal de Investigación Severo Ochoa Programme for Centres of Excellence in R&D (grant no. CEX2019-000917-S). Furthermore, the authors thank D. Alonso-Cerrón Infantes, Fabián A. Amaya-Garcia, and Nick Sokov for fruitful discussions.

## Conflict of Interest

The authors declare no conflict of interest.

## Author Contributions

F.S., H.M., and M.M.U. designed this project. M.M.U. supervised this project. F.S. and M.M.U. wrote manuscript with contributions by all co-authors. F.S. performed all syntheses. Characterizations and the corresponding data analysis were performed by F.S., except for XPS analysis (M.S. and A.F.) and electrochemical testing (T.P. and A.P.). Quantum chemical calculations were performed by L.V. and R.W. All authors have contributed to the writing of the manuscript.

## Data Availability Statement

The data that support the findings of this study are available from the corresponding author upon reasonable request.

## Keywords

hybrid materials, lepidocrocite, pigments, solvothermal syntheses, 2D nanomaterials

Received: February 22, 2024
Revised: May 3, 2024
Published online: July 2, 2024

[1] P. Judeinstein, C. Sanchez, *J. Mater. Chem.* **1996**, *6*, 511.
[2] M. Faustini, L. Nicole, E. Ruiz-Hitzky, C. Sanchez, *Adv. Funct. Mater.* **2018**, *28*, 1704158.
[3] J. D. Mackenzie, D. R. Ulrich, *Sol-Gel Optics* **1990**, *1328*, 2.
[4] R. Reisfeld, D. Brusilovsky, M. Eyal, E. Miron, Z. Burstein, J. Ivri, *Chem. Phys. Lett.* **1989**, *160*, 43.
[5] A. Doménech, M. T. Doménech-Carbó, M. S. del Río, M. L. V. de Agredos Pascual, E. Lima, *New J. Chem.* **2009**, *33*, 2371.
[6] M. Nakamura, H. Nasu, K. Kamiya, *J. Non-Cryst. Solids* **1991**, *135*, 1.
[7] J. S. Lissau, J. M. Gardner, A. Morandeira, *J. Phys. Chem. C* **2011**, *115*, 23226.
[8] Y. Kobayashi, Y. Kurokawa, Y. Imai, S. Muto, *J. Non-Cryst. Solids* **1988**, *105*, 198.
[9] D. Preston, J. C. Pouxviel, T. Novinson, W. C. Kaska, B. Dunn, J. I. Zink, *J. Phys. Chem.* **1990**, *94*, 4167.
[10] M. Quintana, T. Edvinsson, A. Hagfeldt, G. Boschloo, *J. Phys. Chem. C* **2007**, *111*, 1035.
[11] B. O'regan, M. Grätzel, *Nature* **1991**, *353*, 737.
[12] L. Zhang, J. M. Cole, *ACS Appl. Mater. Interfaces* **2015**, *7*, 3427.
[13] H. M. Moura, H. Peterlik, M. M. Unterlass, *J. Mater. Chem. A* **2022**, *10*, 12817.
[14] M. Schneider, K. Müllen, *Chem. Mater.* **2000**, *12*, 352.
[15] X. Wen, S. Fang, Y. Xu, N. Zheng, L. Liu, Z. Xie, F. Würthner, *ACS Appl. Mater. Interfaces* **2019**, *11*, 34151.
[16] Z. Xie, F. Würthner, *Adv. Energy Mater.* **2017**, *7*, 1602573.
[17] M. J. Taublaender, F. Glöcklhofer, M. Marchetti-Deschmann, M. M. Unterlass, *Angew. Chem. Int. Ed.* **2018**, *57*, 12270.
[18] J. B. Dunn, M. L. Burns, S. E. Hunter, P. E. Savage, *J. Supercrit. Fluids* **2003**, *27*, 263.
[19] C. H. Hendon, D. Tiana, M. Fontecave, C. m. Sanchez, L. D'arras, C. Sassoye, L. Rozes, C. Mellot-Draznieks, A. Walsh, *J. Am. Chem. Soc.* **2013**, *135*, 10942.
[20] H. L. Nguyen, F. Gándara, H. Furukawa, T. L. Doan, K. E. Cordova, O. M. Yaghi, *J. Am. Chem. Soc.* **2016**, *138*, 4330.
[21] U. Schubert, *J. Mater. Chem.* **2005**, *15*, 3701.
[22] G. Oskam, A. Nellore, R. L. Penn, P. C. Searson, *J. Phys. Chem. B* **2003**, *107*, 1734.
[23] D. M. Antonelli, J. Y. Ying, *Angew. Chem. Int. Ed.* **1995**, *34*, 2014.
[24] F. Wu, Z. Wang, X. Li, H. Guo, *J. Mater. Chem.* **2011**, *21*, 12675.
[25] J. Schneider, M. Matsuoka, M. Takeuchi, J. Zhang, Y. Horiuchi, M. Anpo, D. W. Bahnemann, *Chem. Rev.* **2014**, *114*, 9919.
[26] H. Choi, E. Stathatos, D. D. Dionysiou, *Desalination* **2007**, *202*, 199.
[27] R. Vadakkekara, R. Illathvalappil, S. Kurungot, *ChemElectroChem* **2018**, *5*, 4000.
[28] D. Xu, Y. Ma, Z. Jing, L. Han, B. Singh, J. Feng, X. Shen, F. Cao, P. Oleynikov, H. Sun, O. Terasaki, S. Che, *Nat. Commun.* **2014**, *5*.
[29] K. G. Reeves, J. Ma, M. Fukunishi, M. Salanne, S. Komaba, D. Dambournet, *ACS Appl. Energy Mater.* **2018**, *1*, 2078.
[30] S. Valencia, X. Vargas, L. Rios, G. Restrepo, J. M. Marín, *J. Photochem. Photobiol. A: Chemistry* **2013**, *251*, 175.
[31] R. Ramirez, S. Zheng, Z. Jiang, S. Wang, M. Yamamoto, US8674103B2, Nitto Denko Corp., **2014**.
[32] J. L. Teteruk, J. Glinnemann, W. Heyse, K. E. Johansson, J. van de Streek, M. U. Schmidt, *Acta Crystallogr., Sect. B: Struct. Sci., Cryst. Eng. Mater.* **2016**, *72*, 416.
[33] Z. Rzaczyńska, R. Mrozek, J. Lenik, M. Sikorska, T. Głowiak, *J. Chem. Crystallogr.* **2000**, *30*, 519.

[34] N. Sundaraganesan, B. D. Joshua, C. Meganathan, R. Meenashi, J. Cornard, *Spectrochim. Acta Part A* **2008**, *70*, 376.
[35] M. Mamada, C. Perez-Bolivar, P. Anzenbacher Jr., *Org. Lett.* **2011**, *13*, 4882.
[36] J. Mizuguchi, *J. Phys. Chem. B* **2004**, *108*, 8926.
[37] N. A. Wasio, R. C. Quardokus, R. D. Brown, R. P. Forrest, C. S. Lent, S. A. Corcelli, J. A. Christie, K. W. Henderson, S. A. Kandel, *J. Phys. Chem. C* **2015**, *119*, 21011.
[38] A. J. Thompson, J. R. Price, J. C. McMurtrie, J. K. Clegg, *Nat. Commun.* **2021**, *12*, 5983.
[39] B. E. Yoldas, *J. Mater. Sci.* **1986**, *21*, 1087.
[40] Z. Bian, J. Zhu, H. Li, *J. Photochem. Photobiol. C* **2016**, *28*, 72.
[41] C.-Y. Wu, K.-J. Tu, J.-P. Deng, Y.-S. Lo, C.-H. Wu, *Materials* **2017**, *10*, 566.
[42] Y. Mao, M. Kanungo, T. Hemraj-Benny, S. S. Wong, *J. Phys. Chem. B* **2006**, *110*, 702.
[43] R. Ma, K. Fukuda, T. Sasaki, M. Osada, Y. Bando, *J. Phys. Chem. B* **2005**, *109*, 6210.
[44] M. Piao, S. M. Oh, J. Lim, S. H. Kim, S.-C. Kim, Y. K. Jo, O. H. Han, S.-J. Hwang, *ACS Appl. Mater. Interfaces* **2018**, *10*, 33112.
[45] C. Zhao, X. Wang, J. Kong, J. M. Ang, P. S. Lee, Z. Liu, X. Lu, *ACS Appl. Mater. Interfaces* **2016**, *8*, 2372.
[46] G. Barim, R. Dhall, E. Arca, T. R. Kuykendall, W. Yin, K. J. Takeuchi, E. S. Takeuchi, A. C. Marschilok, M. M. Doeff, *ACS Appl. Nano Mater.* **2021**, *5*, 678.
[47] T. W. Kim, I. Y. Kim, D.-H. Park, J.-H. Choy, S.-J. Hwang, *Sci. Rep.* **2016**, *6*, 21993.
[48] R. Portela, I. Jansson, S. Suárez, M. Villarroel, B. Sánchez, P. Avila, *Chem. Eng. J.* **2017**, *310*, 560.
[49] M. Fathy, H. Hamad, *RSC Adv.* **2016**, *6*, 7310.
[50] M. Kruk, M. Jaroniec, *Chem. Mater.* **2001**, *13*, 3169.
[51] N. Goujon, M. Lahnsteiner, D. A. Cerrón-Infantes, H. M. Moura, D. Mantione, M. M. Unterlass, D. Mecerreyes, *Mater. Horiz.* **2023**, *10*, 967.
[52] S. Ali, Y. Zhang, H. Yang, T. Xu, Y. Wang, J. Cui, J. E. Ten Elshof, C. Shan, H. Xu, H. Yuan, *ACS Appl. Mater. Interfaces* **2023**, *15*, 5028.
[53] M. Horn, C. Schwebdtfeger, E. Meagher, *Z. Kristallogr. Cryst. Mater.* **1972**, *136*, 273.
[54] D. Zagorac, H. Müller, S. Ruehl, J. Zagorac, S. Rehme, *J. Appl. Crystallogr.* **2019**, *52*, 918.